RESEARCH

α-Mangostin-phytosomes as a plausible nano-vesicular approach for enhancing cytotoxic activity on SKOV-3 ovarian cancer cells

Abdulmohsin J. Alamoudi[1], Shaimaa M. Badr-Eldin[2], Osama A. A. Ahmed[2], Serag Eldin I. Elbehairi[3,4], Mohammad Y. Alfaifi[3], Hani Z. Asfour[5], Gamal A. Mohamed[6], Sabrin R. M. Ibrahim[7], Ashraf B. Abdel-Naim[1] and Hossam M. Abdallah[6*]

Abstract

Background *α*-Mangostin is a major xanthone in *Garcinia mangostana* L. (Clusiaceae) pericarps. It has promising anti-proliferative potential in different cancer cells; however, it has poor oral bioavailability. Phytosomes are used as a novel nano-based drug delivery system. The aim of this research was to enhance the anti-proliferative potency of *α*-mangostin by formulating it as *α*-mangostin-phytosome (*α*-M-PTMs) and assessing its impact on SKOV-3 ovarian cancer cells in comparison to pure *α*-mangostin.

Results The size and entrapment efficiency of the proposed formulation were optimized using Box–Behnken statistics. The optimized formula was characterized using transmission electron microscope. The binding of *α*-mangostin to phospholipids was confirmed using Fourier-transform infrared (FTIR) spectroscopy. The optimized *α*-mangostin-phytosomes formula exhibited enhanced anti-proliferative activity with reference to raw *α*-mangostin. This was further substantiated by assessing the cell cycle phases that indicated an accumulation of SKOV-3 cells in the sub-G1 phase. Annexin-V staining revealed enhanced apoptotic activity in *α*-mangostin-phytosome-treated cells. This was associated with upregulation of CASP3 (Caspase-3), BAX (BCL2 Associated X, Apoptosis Regulator) and TP53 as well as down-regulation of BCL2 mRNA (B-Cell Leukemia/Lymphoma 2). Moreover, our data indicated enhanced ROS (Reactive oxygen species) production, cytochrome-C release, and disturbed MMP (mitochondrial membrane potential).

Conclusion Encapsulation of *α*-mangostin in a phytosome nano-formula enhances its anti-proliferative effects in SKOV-3 cells via, at least in part, inducing mitochondrial apoptotic cell death.

Keywords *α*-Mangostin, *Garcinia mangostana*, Phytosome, SKOV-3, Apoptosis, Caspase, Reactive oxygen species

*Correspondence:
Hossam M. Abdallah
hmafifi@kau.edu.sa
Full list of author information is available at the end of the article

Background

Cancer is characterized by developing aberrant cells that can invade and spread to different bodily regions. Lifestyle plays an important and influential role in cancer incidence. Several factors contribute to cancer incidence, including environmental pollution, carcinogens, mutagens, bacterial and viral infections, and genetic predisposition [1]. By 2035, there will be 14 million cases of cancer among older persons worldwide, doubling the current incidence rate [2].

One of the most serious causes of death among women is ovarian cancer, which is responsible for an increase in gynecological death worldwide. Every year, nearly 300,000 female patients worldwide are diagnosed with ovarian cancer, which is rising [3]. Because of the long time it takes to diagnose ovarian cancer and the poor responsiveness toward the current therapy approaches, the average five-year survival rate is around twenty-five percent [4]. At least 70% of ovarian cancer patients have a poor prognosis and a low survival rate [5, 6]. Patients with ovarian cancer diagnosed at an early stage often have a better prognosis due to the advancement of clinical treatment options, such as surgery, radiotherapy, and chemotherapy. Patients in advanced stages, on the other hand, have a high recurrence rate and a poor prognosis [6].

Garcinia mangostana L. (Clusiaceae) pericarps have been utilized for curing various ailments and possess an array of bioactivities [7–9]. The tree thrives in Malaysia and other hot, humid areas across Southeast Asia, Central America, and Africa. Known for its sweet aril, the fruit's pericarp is utilized in traditional Eastern medicine for treating various conditions like skin infections, urinary tract infections, dysentery, inflammation, abdominal pain, diarrhea, and fevers. The mangosteen plant is primarily abundant in xanthones, alongside benzophenones, tannins, flavonoids, and anthocyanins [8].

α-Mangostin is one of the primary metabolites separated from *G. mangostana* pericarps. It displayed anthelmintic, anti-inflammatory, anti-parasitic, anti-obesity, analgesic, antioxidant, anti-allergic, cardio-, hepato-, and neuro-protective capacities [10]. Additionally, it revealed promising *in-vivo* and *in-vitro* anti-carcinogenic potential versus different cancer types, including lung, colon, skin, pancreas, breast, and blood cancers by affecting various tumor growth phases [11, 12]. It acted by producing apoptosis and growth arrest, mitigating oxidative damage, modulating carcinogenic biotransformation, and prohibiting metastasis and angiogenesis. Further, it diminished the toxic aftereffect and enhanced the effectiveness of the clinically available chemotherapeutics [10, 12].

Boosting the anticancer activity of active moieties has been recently addressed by drug delivery methods based on nanotechnology. A novel approach in nano-based drug delivery is focused on phytosomes (PTMs). The concept of utilizing PTMs in the area of drug delivery was introduced in the early 90 s. Phytosomes refer to complexes formed by the interaction between plant-derived active components and the polar head of phospholipids via hydrogen bonding [13]. These interactions facilitate the incorporation of the active ingredients into the complexes, wherein the phospholipid head group acts as an anchor, while the two elongated fatty acid chains do not actively engage in the process of complex formation. The fatty acid chains can undergo movement and enclose the polar segment of the complexes, generating a surface that exhibits lipophilic properties. One notable differentiation between phytosomes and liposomes lies in the way the active ingredient is incorporated. In liposomes, the active ingredient is dispersed within the cavity or membrane layers. Conversely, in phytosomes, the active ingredient is an intrinsic constituent of the membrane, forming hydrogen bonds with the polar head of the phospholipids [14]. Such a unique complex structure of PTMs could infer clinical advantages, including enhancing cellular uptake and biological activity of ingredients [15].

The current investigation's objective was to delve into the potential of this innovative, promising nanocarrier platform for enhancing the cytotoxicity of *α*-mangostin. Accordingly, Box–Behnken statistical analysis optimized the proposed formulation concerning size, PDI (polydispersity index), and EE% (entrapment efficiency). Additionally, comprehensive testing of the tailored formulation on SKOV-3 cell lines was performed to assess its effectiveness against ovarian cancer.

Methods

Isolation of α-mangostin

α-Mangostin was isolated from *Garcinia mangostana* fruits that were purchased from local market in Saudi Arabia. The identity of the plant was confirmed by staff members of Natural products Department, Faculty of Pharmacy, King Abdulaziz University and it was kept at the herbarium (GM-1424). Scheme of *α*-mangostin isolation is presented in Fig. 1**.** The compound was identified by co-TLC with authentic sample, as well as comparing its ^{1}H and ^{13}C NMR data (Figures S1-2, Table S1) with literature [8].

Design of experiments

A central face-centered composite response surface design optimized *α*-M-PTMs. The design aimed at exploring the influence of two independent formulation variables, namely *α*-mangostin to phospholipid (PL;
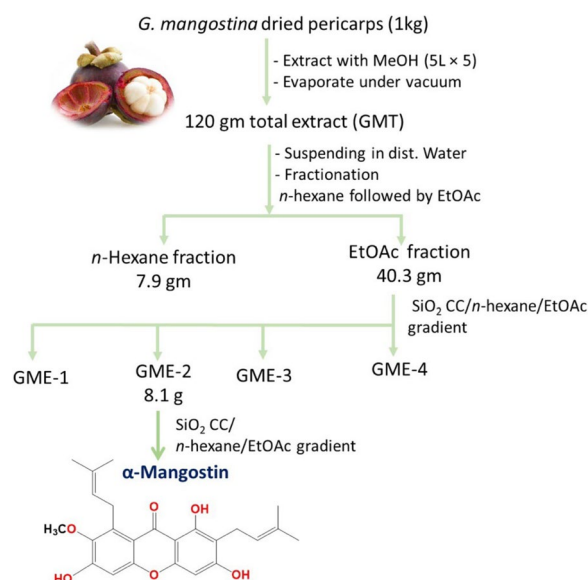
Alamoudi *et al. Future Journal of Pharmaceutical Sciences*   (2024) 10:143

Page 3 of 19

Fig. 1 Schematic presentation of purification of *α*-mangostin from *G. mangostana*

Table 1 Formulation variables and responses constraints utilized to formulate and optimize *α*-M-PTMs in the Box-Behnken design

Independent variables	Levels		
	(−1)	(0)	(+1)
X_1: *α*-M: PL molar ratio	1:1	1:2.5	1:4
X_2: Process temperature (℃)	45	55	65
Responses	Desirability constraints		
Y_1: Vesicle size (nm)	Minimize		
Y_2: Polydispersity index	Minimize		
Y_3: Entrapment efficiency (%)	Maximize		

Phospholipon-90G phospholipid (PL) kindly supplied by Lipoid GmbH-Koln-Germany) molar ratio (*α*-M: PL, X_1) and process temperature (Temp, ℃, X_2), on three selected responses, namely, entrapment efficiency (EE, Y_3, %), polydispersity index (PDI, Y_2), and vesicle size (Y_1, nm). The variables levels and the set goals for the selected responses are listed (Table 1). Design-Expert software produced 13 runs with various combinations of the variable values (version 12; Stat-Ease Inc.-Minneapolis-MN-USA) in accordance with the design in use, as indicated in Table 2. The least PRESS (predicted-residual sum of squares) and the predicted and adjusted determination coefficients were computed to find the best-fitting model for the observed responses. Adequate precision was used as an indicator for the model's appropriateness. Analyzing the observed responses statistically was conducted using ANOVA (analysis of variance). The perturbation plots were generated to show the main variables' impacts, whereas contour and response plots were generated to represent the interaction between them.

Preparation of α-M-PTMs

As per the experimental runs specified molar ratios, *α*-M and PL amounts were accurately weighed, and mixed with organic solvent (chloroform: methanol 10:1) at room temperature until it was a clear solution. Then, the organic solvent was evaporated at 150 rpm for 30 min at the specified temperature (according to the experimental design runs). Following a 48-h lyophilization process of the concentrate, the dried PTMs were then kept in amber-glass containers at 4 ℃ until additional investigation.

PDI and vesicle sizes assessment

α-M-PTMs were dispersed using deionized water, and the dynamic light scattering (DLS) technique was implemented for assessing PDI (polydispersity index) and vesicular size as z-average using Nano-ZSP Zetasizer (Malvern Panalytical Ltd._Malvern_UK). The size of each sample was measured five times at ambient temperature; results are presented as mean ± standard deviation.

EE% determination

In brief, 0.1% Triton×100 was utilized to lyze an accurately weighed quantity of the PTMs formulation. After appropriate dilution with ethanol, *α*-M was quantified using UV–Vis spectrophotometry at 317 nm [16].

Optimization

A numerical technique using the desirability function, which aggregates all responses into a single parameter, was employed to optimize *α*-M-PTMs. The optimal levels of the explored independent variables were predicted to achieve the set goals of minimizing vesicle size and PDI and maximizing EE. The optimal formulation was developed for further research.

Characterization of the optimized α-M-PTMs

Using the Nano-ZSP Zetasizer, the improved formulation's zeta potential was determined (Malvern Panalytical Ltd. Malvern_UK) to assess the stability against aggregation. Further, the shape of the optimized formulation was assessed using JEM-1400 TEM at 80 kV (JEOL Ltd. Tokyo-Japan). One drop of the *α*-M-PTMs sample was applied to a carbon-coated grid, left to dry, and subsequently negatively stained phosphotungstic acid 1% (Fisher Scientific, Pennsylvania, USA). Before visualization, the material was dried for 15 min at room temperature.

Table 2 Independent variables levels and the corresponding responses (measured) for *α*-M-PTMs runs were constructed according to the central composite design

Run no	Independent variables		Response		
	A-**M: PL molar ratio**	Process Temp. (℃)	**Vesicle size (nm) ± SD***	**Polydispersity index**	**Entrapment efficiency (%) ± SD#**
SDF1	1:2.5	65	149.5 ± 4.8	0.221	93.9 ± 3.9
F2	1:4	65	206.4 ± 9.2	0.217	96.7 ± 3.4
F3	1:1	45	235.1 ± 9.9	0.292	85.5 ± 2.6
F4	1:2.5	55	193.1 ± 7.9	0.297	91.3 ± 3.8
F5	1:2.5	55	187.5 ± 7.1	0.275	90.3 ± 3.2
F6	1:2.5	55	192.7 ± 6.8	0.292	90.7 ± 3.2
F7	1:2.5	55	193.4 ± 6.2	0.293	91.6 ± 3.7
F8	1:2.5	45	279.4 ± 12.1	0.322	86.9 ± 2.8
F9	1:4	45	327.3 ± 13.6	0.417	89.7 ± 2.6
F10	1:4	55	249.1 ± 9.6	0.321	94.7 ± 2.9
F11	1:1	65	103.2 ± 3.2	0.209	91.8 ± 3.1
F12	1:1	55	138.6 ± 5.8	0.241	88.9 ± 2.9
F13	1:2.5	55	192.6 ± 6.9	0.291	91.9 ± 3.1

*Results are presented as mean ± SD; n = 5

Results are presented as mean ± SD; n = 3

FTIR (Fourier-transform infrared) spectroscopy measurement

The interaction between *α*-mangostin and phytosmes was confirmed by measuring FTIR spectra of *α*-mangostin, phytosomes, their physical mixture and the optimized prepared formula in the range of 400–4000 cm^{-1} utilizing FTIR spectro-photometer (TENSOR37, Bruker, Germany).

Cell Culture

SKOV 3 and EA.hy926 (human umbilical vein) cell lines were obtained from NAWAH Scientific (Cairo, Egypt) and NCCS (Pune/India). DMEM (Dulbecco's Modified-Eagle's Medium, Gibco-Montana-USA) was used to culture human ovary tumor cells (SKOV 3) cell lines supplemented with streptomycin/penicillin 50 units/mL and 10% Fetal bovine serum (FBS) (Fisher Scientific, Pennsylvania, USA). The cells were kept in a humid environment with 5% CO_2 at 37 ℃.

Assay of cell viability

SKOV-3 cells were seeded in 96-well plates at a density of 8 X 10^3 cells per well and rinsed with acetic acid 1% three times (Merck-Rahway, New Jersey, United States) and allowed to air dry for an entire night. After 48 h of exposure to PL, *α*-M, *α*-M-PTMs, and doxorubicin (positive control), the media were changed with 10% trichloro acetic acid (TCA) (150 µL) of (Merck-Rahway-New Jersey-United States) for 1 h at 4 ℃. This was followed by 5-times washing with distilled H_2O. Next, sulforhodamine B (SRB) solution (50 µL; 0.4%w/v in acetic acid) (Sigma Aldrich, St. Louis, Missouri, USA) was added and allowed to sit for 10 min at room temperature in a dark location [17]. Protein-bound SRB stain was dissolved in Tris Base 10 mM (150 mL; Merck, Rahway, NJ, USA). The optical density was calculated at 540 nm employing a microplate reader. In the meanwhile, to determine their safety, EA.hy926 (human umbilical vein) cells were grown in DMEM and treated with various concentrations of *α*-M and *α*-M-PTMs [17].

Cell cycle analysis

Data from 10,000 cells and the cell cycle phases` distribution for each sample were examined employing SpectroFloTM Software (version 2.2.0.3, Cytek Biosciences, California, USA). For 48 h, PL, *α*-M, and *α*-M-PTMs at their IC_{50} values were incubated with SKOV-3 cells. After trypsinization, the cells were twice washed in PBS (phosphate-buffered saline), fixed in 60% ice-cold ethanol at 40 ℃ and then again in PBS. After being suspended once more in 500 µL PI (propidium iodide) with RNase-staining buffer (Cell Signaling Technology), the cells were incubated for a duration of 15 min. Lastly, a Cytek® Northern Lights-2000 spectral flow cytometer (Cytek Biosciences, California, USA) was applied to perform the FACS (Fluorescence-activated cell sorting) assessment [18].

Annexin V staining

According to the supplier, apoptosis analysis was carried out by the Apoptosis detector; Annexin V-FITC/PI Kit (CST Inc., Danvers, Massachusetts, USA). Following a 48 h treatment with PL, α-M, and α-M-PTMs, SKOV-3 were trypsinized and thrice washed with PBS. To summarize, the cells were suspended again in 5 μl Annexin V-FITC, to which 5 μL PI was added before 0.5 ml binding buffer with gentle stirring for 15 min in a dark area at room temperature. Finally, FACS examination was done employing a Cytek® Northern Lights-2000 spectral flow cytometer and Spectro-Flo™ Software (version 2.2.0.3, Cytek-Biosciences, California-USA) [19, 20].

BAX, TP53, CASP3, and BCL2 mRNA expression

An average of 1×10^6 SKOV 3 cells were seeded and incubated in an atmosphere of 5% CO_2 for 24 h at 37 °C to reach 70% confluence. The next day, the cells were treated with the calculated IC_{50} for PL, α-M, and α-M-PTMs. In addition, the carrier solvent (0.1% DMSO) was used for control cells, and the treated cancer cells were incubated in an atmosphere of 5% CO_2 for 48 h at 37 °C. Using real-time PCR (polymerase chain reaction); BAX (BCL2 Associated X, Apoptosis Regulator), TP53 (Tumor protein p53), BCL2 (B-Cell Leukemia/Lymphoma 2), and CASP3 (Caspase-3) mRNA expression was assessed in treated cells. RNeasy Mini-Kit (Qiagen-Hilden-Germany) was employed to extract total mRNA in accordance with the manufacturer's guidelines.

Reverse transcription reaction was used to create cDNA utilizing the Quantitect RT Kit (Qiagen, Hilden, Germany). BCL2, TP53, BAX, and CASP3 mRNAs were amplified from total RNA extracts employing the TP53 (QT00060235), BCL2 (QT0025011), CASP3 (QT00023947), BAX (QT00031192) and β-actin (QT000954231) primers (Qiagen, Hilden, Germany) and Quantitect Syber-green Master-mix (Qiagen, Hilden, Germany). β-actin mRNA was used as a housekeeper gene. The 5plex 5plex-Rotor-Gene PCR Analyzer (Qiagen-Hilden- Germany) was used to analyze each sample in triplicate. The $2^{\Delta\Delta Ct}$ technique was used to measure the gene expression levels, and β-actin, an endogenous reference control, was utilized to normalize the results [21].

Assessment of ROS generation

ROS (reactive oxygen species) was assessed in the collected cells 48 h after treatment with the IC_{50} of PL, α-M, and α-M-PTMs using the ELIZA technique. The human reactive oxygen species (ROS) ELISA Kit (Cat. No: MBS3800709, MyBioSource, San Diego, California, USA). The test was carried out in accordance with the directions given by the manufacturer.

Assessment of MMP

MMP was assessed utilizing the MMP Assay Kit (Cat. No: ab112150, Abcam- Cambridge, UK) in accordance with the instructions given by the manufacturer.

Assessment of cytochrome c concentration

Human Cyt-C (Cytochrome-C) ELISA Kit (Cat. No.: E-EL-H0056, Elabscience-Biotechnology, Houston, Texas, USA) was used in accordance with the manufacturer's recommendations to measure cytochrome c release in harvested cells using the ELISA technique.

Statistical analysis

The data is shown as mean ± SD. Statistical analysis, including multiple comparisons, was performed using GraphPad Prism version 9 (San Diego, CA, USA). One-way ANOVA with Tukey's post-hoc test was conducted, with statistical significance defined as $p < 0.05$.

Results

Statistics of model fit

Table 3 provides a summary of the fit statistical analysis findings for the measured responses. According to the lowest PRESS and the highest computed R^2, the selected polynomial models were quadratic, two-factor interaction (2FI), and linear for vesicle size, PDI, and EE, respectively. The adequate precision values were 97.21, 28.96, and 30.24 for vesicle size, PDI, and EE, respectively. In addition, the lack of fit P-values was greater than 0.1 for all models.

Diagnostic plots were produced to evaluate the models' degree of fit (Fig. 2). Figure 2A–C illustrates the externally studentized residuals vs. predicted values showing randomly scattered dots within limits. Figure 2D–F, illustrating actual vs expected values for the three responses, exhibited high linearity.

Table 3 α -M PTMs responses fit summary statistics on the basis of best fitting model

Response	Model	Sequential *P*-value	Lack-of-fit *P*-value	R^2	Adjusted (R^2)	Predicted (R^2)	PRESS
Vesicle size	Quadratic	< 0.0001	0.1378	0.9980	0.9966	0.9847	644.36
Polydispersity index	2FI	0.0011	0.1514	0.9626	0.9502	0.9039	0.0035
Entrapment- efficiency	Linear	< 0.0001	0.4931	0.9593	0.9512	0.9340	7.27
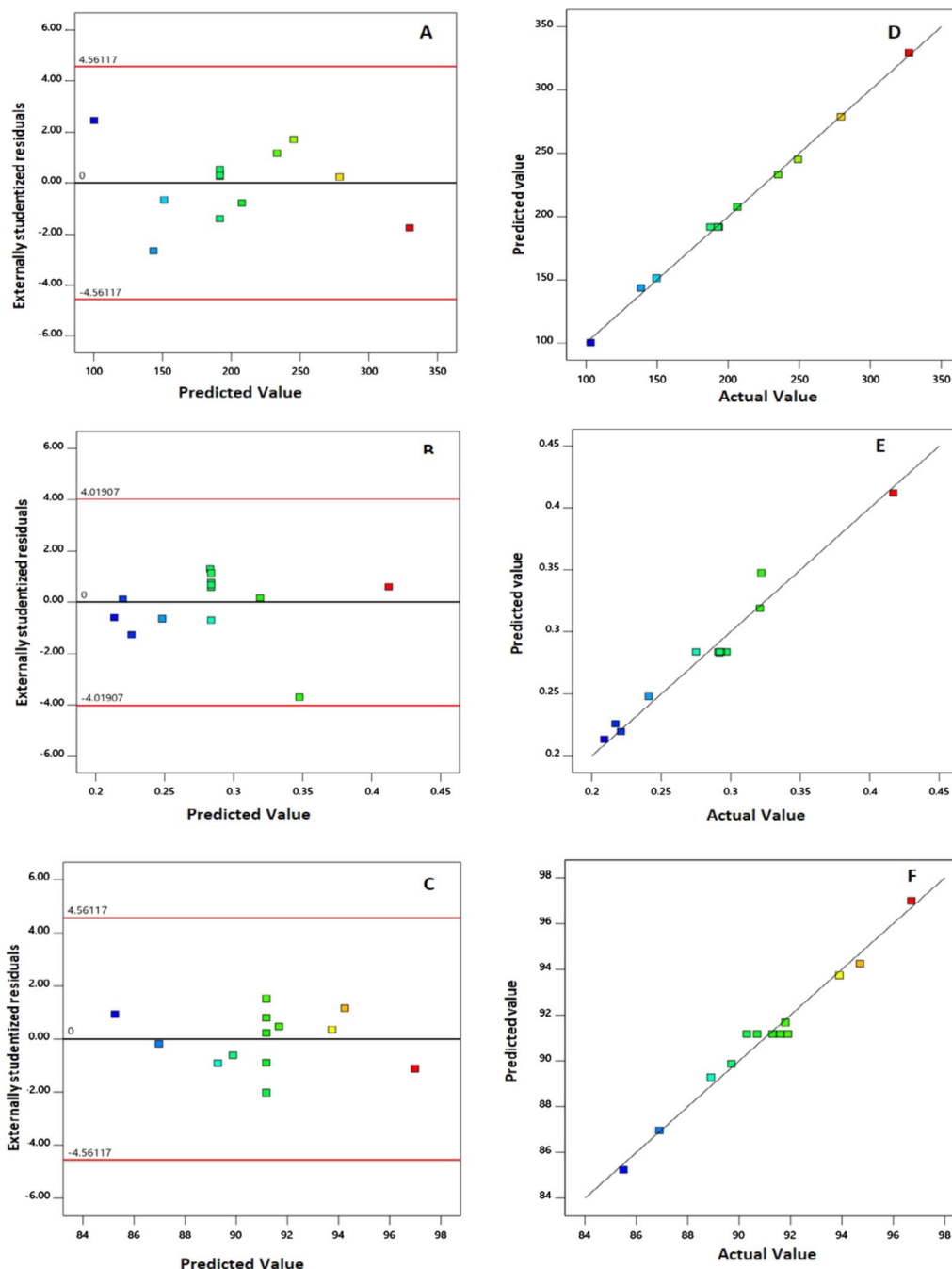
Fig. 2 Diagnostic plots for (**A**, **D**) vesicle size, (**R**, **E**) PDI, and (**C**, **F**) EE% of α-M-PTMs. (A-C) Externally-studentized residuals vs. predicted values plots, (D-F) predicted versus Actual responses

Variables influence the vesicle size (Y_1)

The prepared α-M-PTMs showed sizes ranging from 103.2 ± 3.2 to 327.3 ± 13.6 nm (Table 2). With an F-value of 695.11 ($P < 0.0001$), ANOVA for vesicle size demonstrated the applicability of the quadratic model. In terms of the coded factors, the following equation was created to represent the quadratic model that fit the data the best:

$$Y_1 = 191.64 + 50.98\,X_1$$
$$- 63.78\,X_2 + 2.75\,X_1 X_2$$
$$+ 2.74\,X_1^2 + 23.34\,X_2^2$$

Both α-M:PL molar ratio and process temperature have significantly influenced the vesicle size as presented by a P value < 0.0001 for their corresponding quadratic term

X_2^2 and linear terms X_1 and X_2. The impact of both variables on the vesicle size is demonstrated by the perturbation plot shown in Fig. 3A. Further, the 2D-contour and 3D-surface plots in Fig. 4A and 4B illustrate their interaction. The size is directly proportional to the α-M:PL molar ratio and inversely proportional to the process temperature.
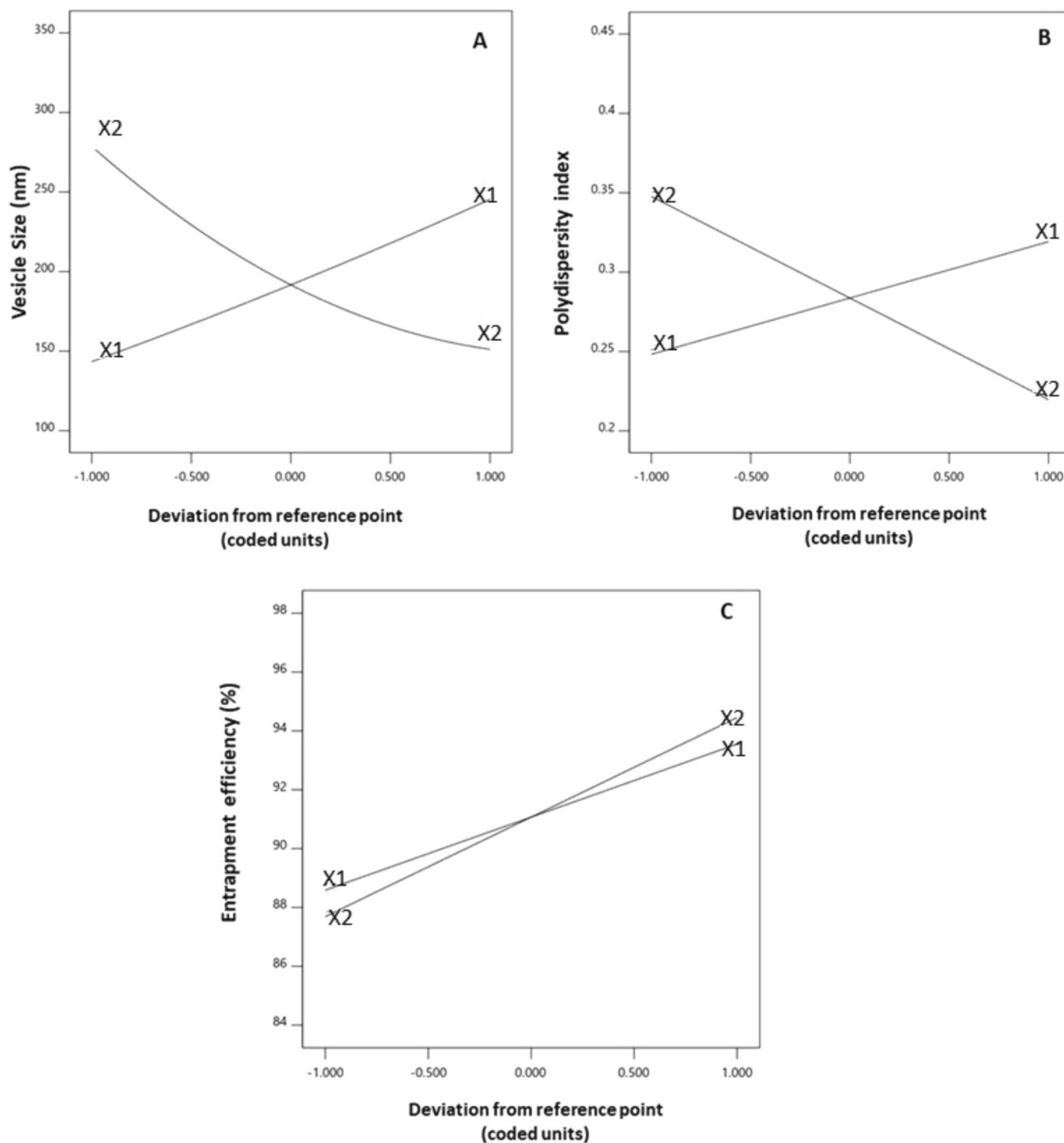

Fig. 3 Perturbation plots for the main effects of α-M: PL molar ratio (X_1) and process temperature (X_2) on the size (**A**), PDI (**B**), and EE% (**C**) of α-M-PTMs
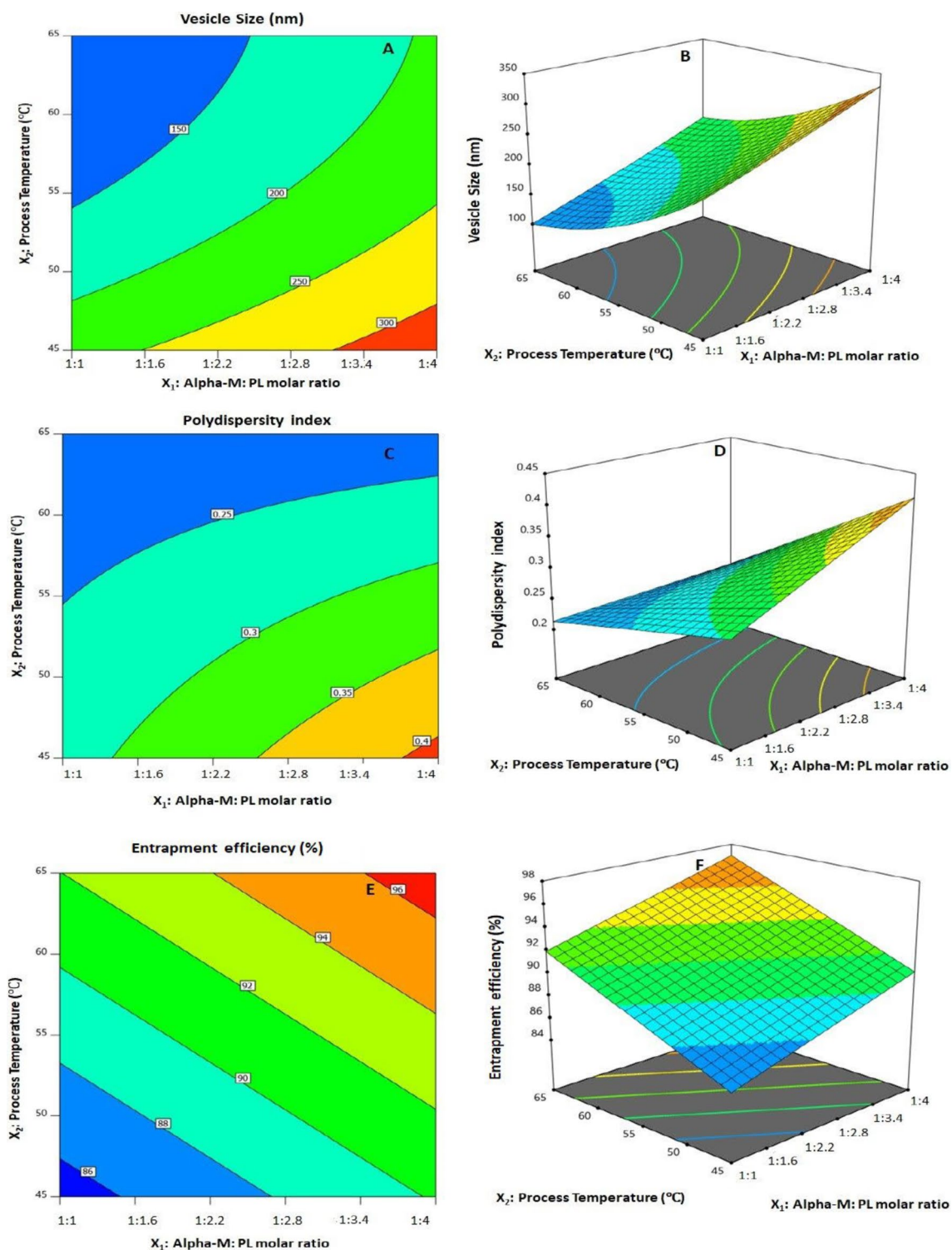
Fig. 4 Response surface plots for the interaction between α-M: PL molar ratio (X_1) and process temperature (X_2) on the **A**–**B** size, **C**–**D** PDI, and **E**–**F** EE% of *α* -M-PTMs. 2D-contour plots *(*A, C, E); 3D-surface plots (B, D, F)

Variables influence on PDI (Y$_2$)

The prepared α-M-PTMs showed fair PDI values that range from 0.209 to 0.417 (Table 2). ANOVA for PDI confirmed that the data fitted the 2FI model, with an *F*-value of 77.25 ($P = 0.0011$), and the following coded factor equation was produced.

$$Y_2 = 0.2837 + 0.0355\,X_1 - 0.0640\,X_2 - 0.0292\,X_1X_2$$

According to ANOVA results, both α-M: PL molar ratio and process temperature and the interaction between the two factors were significant on the PDI ($P < 0.0001$ for X_1 and X_2 and $P = 0.0011$ for X_1X_2). The plot in Fig. 3B shows the influence of both variables on PDI, while the contour and surface plots presented in Fig. 4C, D illustrate the interaction between them. The influence of the factors on the PDI is congruent to their impact on the particle size; the homogeneity of the dispersions is inversely related to the vesicle size. The PDI increases as the size increases, indicating decreased homogeneity and vice versa.

Variables influence EE% (Y$_3$)

The prepared α-M-PTMs exhibited acceptable EE% values that exceeded 85% (Table 2). ANOVA for EE% supports the fitting to the linear model, evidenced by an *F*-value of 117.84 ($P < 0.0001$), and the following coded factor equation was produced.

$$Y_3 = 91.07 + 2.48\,X_1 + 3.38\,X_2$$

According to the ANOVA analysis, both investigated variables significantly influence the EE% ($P < 0.0001$ for both X_1 and X_2 corresponding to α-M: PL molar ratio and process temperature, respectively. Figure 3C illustrates the impact of both variables on the EE%, while the contour and surface plots are presented in Fig. 4D, F, respectively, confirm the absence of any interaction between them.

Optimization

The levels of the optimized variables, when combined, should result in reduced size and PDI with maximized EE% were predicted using the desirability approach and the numerical technique. The ramp graphs in Fig. 5A showed both the optimal values and the expected outcomes. Figure 5B displays each response's overall desirability values and desirability ratings. The measured size, PDI, and EE% of the optimized formulation were 138.9 nm, 0.221, and 95.1%, respectively.

Characterization of the optimized α-M-PTMs

The optimized formulation was further characterized for zeta potential and shape. The optimized formulation's mean zeta potential was -44.5 ± 1.5 mV. The TEM investigation's findings for the α-M-PTMs optimized formula revealed almost spherical entities (Fig. 6). Given that the vesicle size was reduced in the TEM study due to the drying process that the sample was put through to prepare for the TEM imaging, the vesicle size was comparable to the size data received from the particles size analyzer.

FTIR spectroscopy study

The IR spectrum of α-mangostin showed a sharp peak at 3420 cm^{-1} and another wider one around 3253 cm^{-1} representing stretching vibration of hydroxyl groups ($-$OH), multiple weak peaks before 3000 cm^{-1} at 2989, 2962, 2855 cm^{-1} for aliphatic side chains (Fig. 7). The stretching vibration of cyclic conjugated Carbonyl (C=O) group appears as very sharp peak around 1643 cm^{-1} which coupled with 1611 cm^{-1} for stretching vibration of unconjugated aliphatic C=C while aromatic conjugated (C=C) of aromatic nature showed a sharp broad band around 1583 cm^{-1}. The aliphatic $-$CH$_2$ and -CH$_3$ bending vibrations represented strong peaks around 1376 cm^{-1}. The band around 1096–1239 cm^{-1} revealed the (C–O) stretching vibrations.

The FTIR spectra of PL showed peaks at 2956 and 2917 cm^{-1} for asymmetric stretching vibrations of methyl and methylene groups of fatty acid. Moreover, it displayed two bands for the two carbonyl ester groups at 1739 and 1643 cm^{-1}. The aliphatic methyl and methylene bending vibrations represented strong peaks around 1378 cm^{-1}. In addition, the spectra displayed band at 1238 cm^{-1} for P=O stretching peaks and at 1061 cm^{-1} for C–O–P stretching and band at 968 cm^{-1}- for N$^+$(CH$_3$)$_3$ stretching.

The physical mixture showed both peaks of α-mangostin and PL in the spectra; and remained consistent with a negligible shift from original scale, showing that they were not involved in the development of a complex or even any types of interactions. The FTIR spectrum of α-M-PTMs (Fig. 7) augmented the interaction between α-mangostin, and PL through appearance of peaks at 3391 cm^{-1} for hydroxyl groups that could be attributed to inclusion of the hydroxyl groups α-mangostin (H-bond donors) in hydrogen bonding with electronegative O-atoms of esters of PL (H-bond acceptor). Moreover, the -CH$_2$- and -CH$_3$ groups of aliphatic side chains of both α-mangostin and PL are still represented at 2925–2854 cm^{-1} with bands wider and more increased intensity that they may be engaged together by non-polar forces of attractions, e.g., Van der Waal force. Finally, the broadness and less sharpness of peak around 1738 cm^{-1} may refer to the complete overlap between two regions of carbonylic esters (C=O) of α-M-PTMs due to encountered at
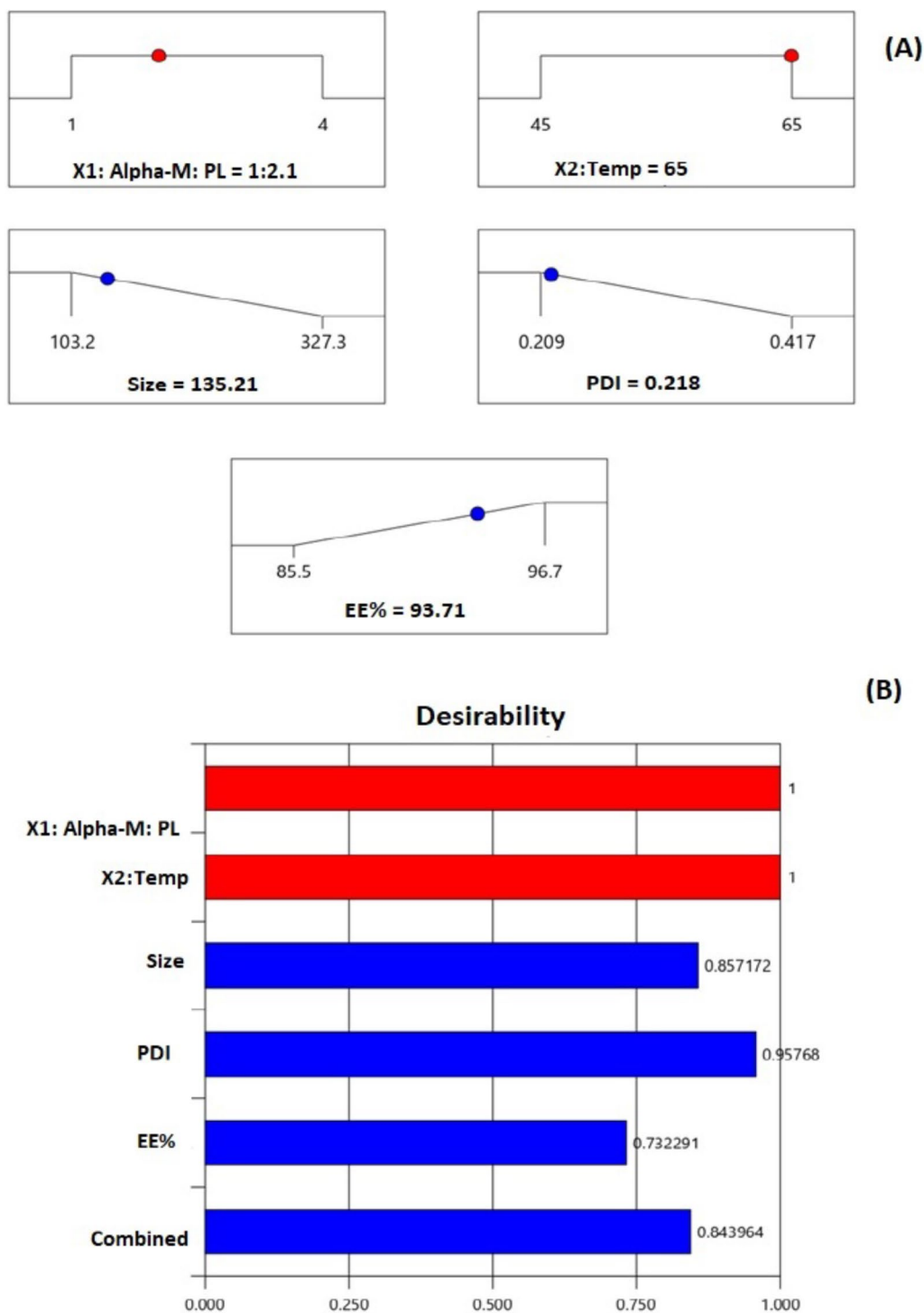
Fig. 5 **A** Ramp graphs represent the predicted responses and independent variables' optimized levels for the optimized α-M-PTMs. **B** Desirability values for the expected responses and optimized α-M-PTMs overall desirability

intermolecular hydrogen bonding. Thus, they also participate in stabilization of intermolecular H-bonding as H-Bond acceptor.

Antiproliferative activity

In the cytotoxic assay, the α-M-PTMs were evaluated against human ovary tumor cells, SKOV 3, for their
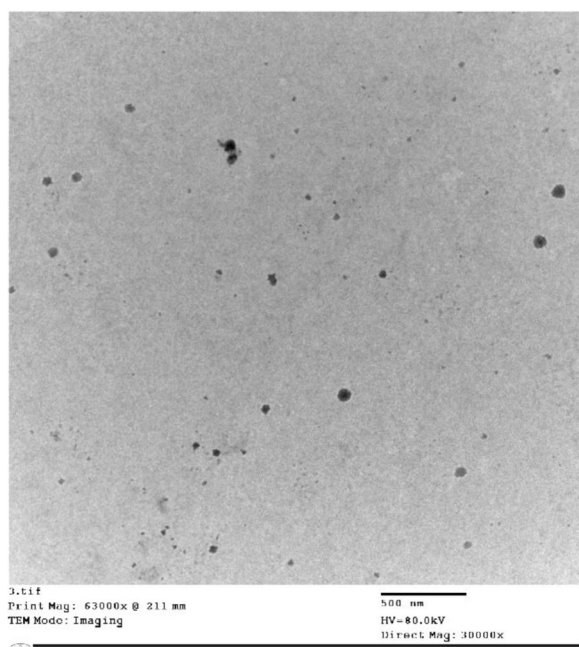
Fig. 6 TEM image of the optimized *α*-M-PTMs formulation

cytotoxic effects. *α*-M-PTMs had a significantly improved cytotoxic profile with an IC_{50} of 2.14 µg/ml compared to the *α*-M cytotoxic effect, which had an IC_{50} of 5.90 µg/ml (Fig. 8). Interestingly, the cytotoxic effect of the PL (representing blank PTMs) was relatively low, with an

IC_{50} value of 57.36 µg/ml. On the other hand, the positive control doxorubicin expressed significant cytotoxic activity with an IC_{50} of 0.26 µg/ml (Fig. 8). The results indicate that the IC_{50} value of *α*-M was reduced by about 64% when loaded into the PTMs. The cytotoxic activity of the improved formula against non-cancerous endothelial cells, EA.hy926 was found to be relatively weak. PL, *α*-M, and *α*-M-PTMs preparations exhibited IC_{50} values of 82.8, 36.6, and 16.2 µg/ml, respectively, against EA.hy926 cells.

Analysis of cell cycle

Arrest of the cell cycle is one of the most common causes of cell growth suppression. Hence, the SKOV-3 cell line was treated with PL, *α*-M, and *α*-M-PTMs at their IC_{50} concentrations to examine whether the observed cellular growth inhibition is caused by cell cycle arrest. Figure 9 shows a significant population of SKOV 3 cells found in the sub-G1 cell cycle stage upon treatment with *α*-M-PTMs compared to the control. There was also a raise in cell population in the sub-G1 phase accompanied with the PL and *α*-M treatments; however, neither PL nor *α*-M significantly increased the SKOV 3 cell population to the levels observed with the *α*-M-PTM treatment. Further, *α*-M significantly caused S phase cell cycle arrest.

Assessment of annexin V staining

The percentage of SKOV-3 cells undergoing apoptosis or necrosis following the different treatments was
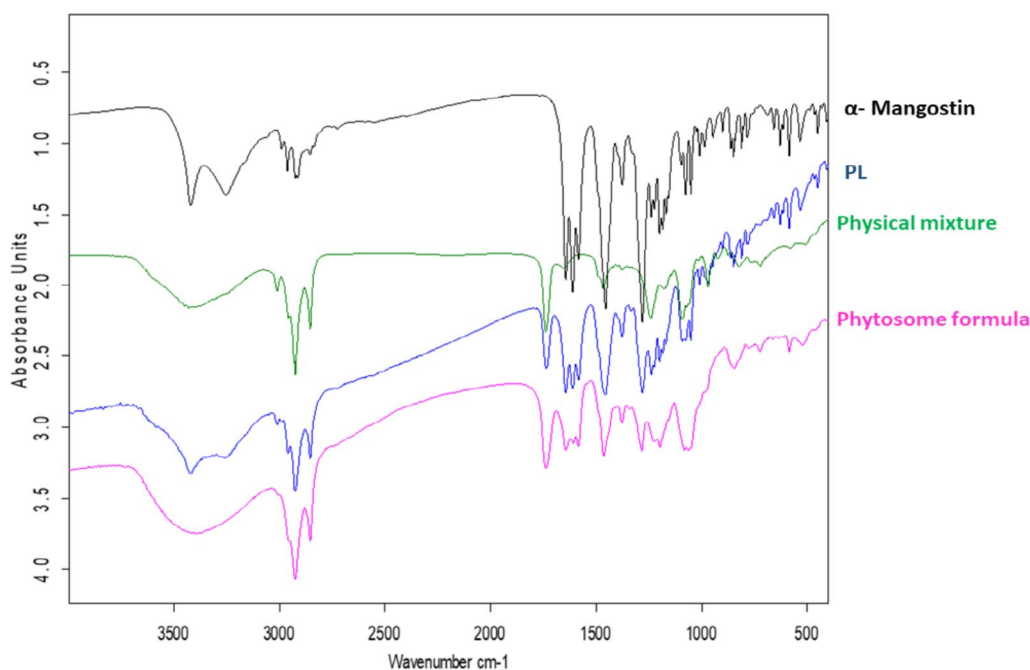

Fig. 7 Fourier-transform infrared (FTIR) of *α*-Mangostin, PL, physical mixture and *α*-M-PTMs
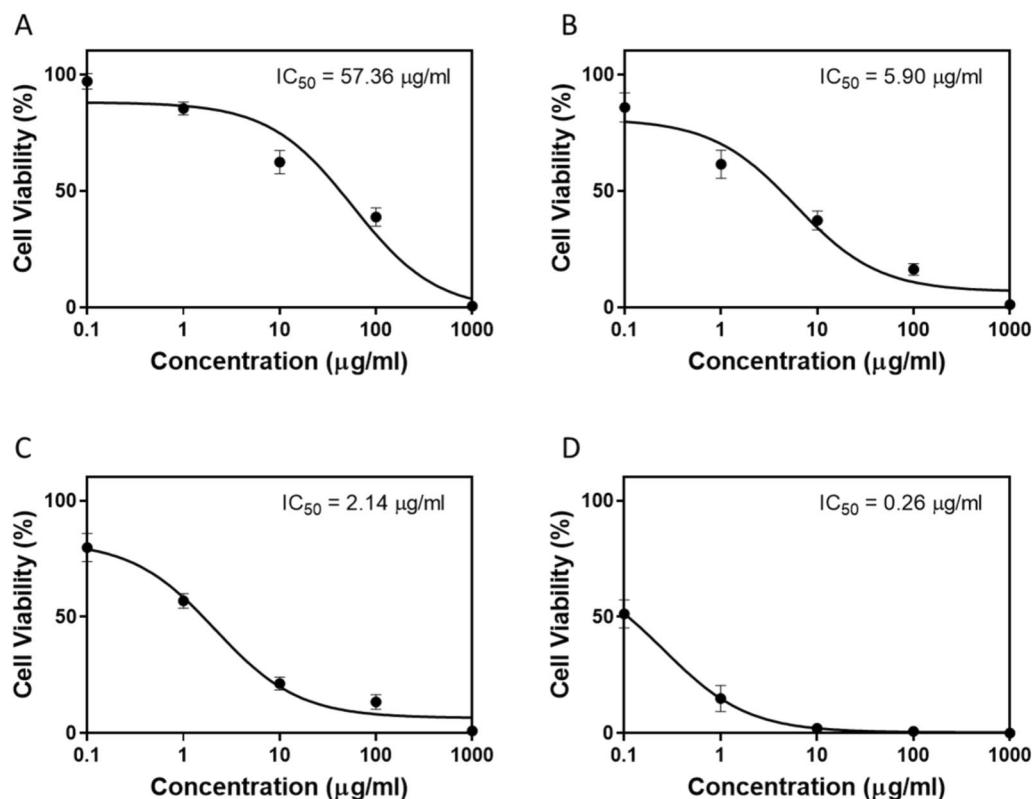
Fig. 8 The cytotoxicity dose–response curves and IC$_{50}$ values of PL (**A**), *α*-M (**B**), *α*-M-PTMs (**C**), and doxorubicin (**D**) against SKOV-3 cells exposed to tenfold dilutions of the compounds for 48 h

ascertained employing annexin V in conjunction with PI (propidium iodide) labeling. Compared to the control, PL, and *α*-M groups, *α*-M-PTMs notably raised late apoptotic cell counts in SKOV 3 cells by 202, 386, and 491%, respectively. Regarding necrosis, *α*-M and *α*-M-PTMs treatments had significant necrotic effects on cancer cells compared to the control (Fig. 10).

BAX, CASP3, TP53, and BCL2 mRNA expression
Apoptosis in SKOV-3 cells was also assessed using qPCR analyses. The *α*-M -PTMs-treated cells had significantly higher levels of the proteolytic enzyme CASP3 than the control cells and those treated with PL or *α*-M (Fig. 11). Moreover, the analysis showed that *α*-M-PTM had caused significantly lower mRNA levels of the antiapoptotic protein BCL2 but higher mRNA expression levels of the pro-apoptotic regulators BAX and TP53 compared to the control values (Fig. 11). The apoptotic effects of *α*-M were similar to those of *α*-M PTMs, yet with significantly lower intensities. Finally, PL had limited impacts on the expression of apoptotic genes in the treated cells (Fig. 11).

Assessment of ROS production, cytochrome C release, and MMP
To determine whether the apoptotic effects of *α*-M-PTMs are linked to oxidative stress, ROS levels were evaluated in the treated SKOV-3 cells. The results showed that *α*-M and *α*-M-PTMs caused a significant increase in ROS production in SKOV-3 cells, while PL exhibited ROS levels comparable to the control (Fig. 12). The effect of *α*-M-PTMs on MMP was then evaluated on the SKOV-3 cells. The results show that the fluorescence intensity significantly decreased by 68% and 71% in cells treated with *α*-M and *α*-M-PTMs compared to the control group, indicating disrupted MMP. However, treatment with PL resulted in no notable variations in MMP to the control level (Fig. 12). Finally, cytochrome c concentration was also determined across the different treatment groups. The results show that the release of cytochrome c was significantly increased by 231% in *α*-M-PTMs-treated cells compared to the control values (Fig. 12). Similarly, *α*-M and PL increased the cytochrome c release by 166% and 24%, respectively.
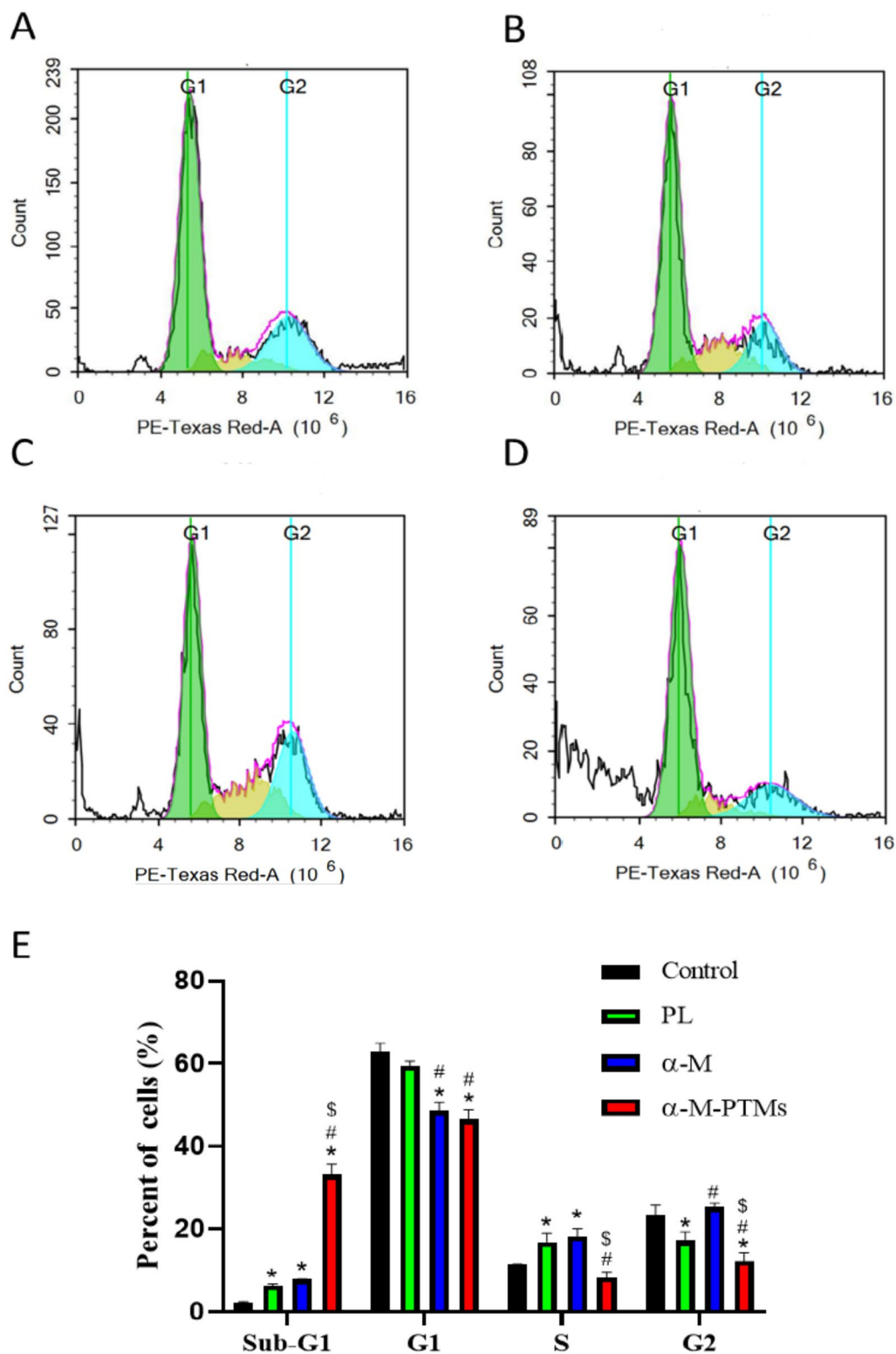
Fig. 9 Cell cycle distribution of SKOV 3 cells after a 48 h-treatment by the control (**A**), PL (**B**), *α*-M (**C**), *α*-M-PTMs (**D**), and the quantification of cells at each cell cycle phase (E). Data (*n* = 3) is represented as mean ± SD. *: Significantly varied from control ($p < 0.05$); #: significantly varied from PL ($p < 0.05$); $: significantly varied from *α*-M ($p < 0.05$)

Fig. 10 Effect of the control (**A**), PL (**B**), *α*-M (**C**), *α*-M-PTMs (**D**), and the quantification of cells undergoing late and early apoptosis and necrosis (**E**) in SKOV 3 cells. Exposure to treatments for 48 h. Data are presented as mean ± SD ($n = 3$). *: Significantly varied from control ($p < 0.05$); #: significantly varied from PL ($p < 0.05$); $: significantly varied from *α*-M ($p < 0.05$)
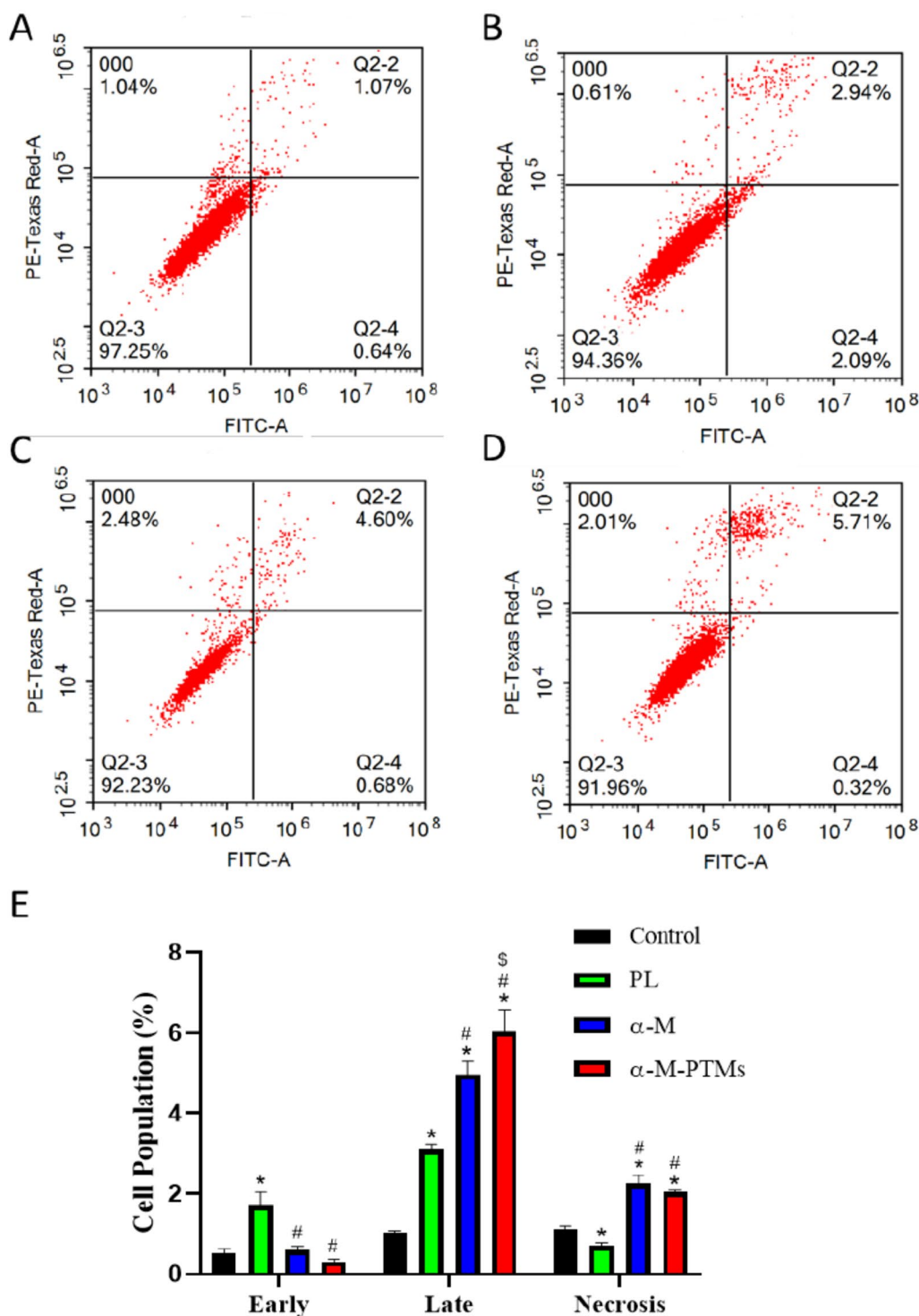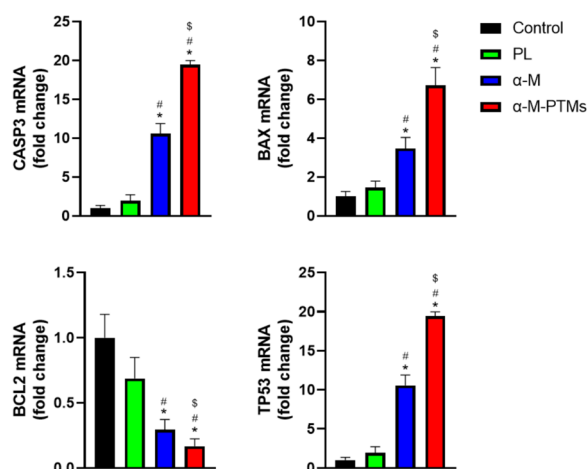
Fig. 11 CASP3, BAX, BCL2, and TP53 mRNAs were expressed following treatment with the control, PL, *α*-M, and *α*-M-PTMs in SKOV 3 cells. Exposure to treatments for 48 h. Data are presented as mean ± SD; *n* = 3. *: Significantly varied from control ($p < 0.05$); #: significantly varied from PL ($p < 0.05$); $: significantly varied from *a*-M ($p < 0.05$)

Fig. 12 Effect of PL, *α*-M, and *a*-M-PTMs on the generation of ROS, MMP, and the cytochrome c cytosolic release in SKOV 3 cells. Exposure to treatments for 48 h. Data are presented as mean ± SD; *n* = 3. *: Significantly varied from control ($p < 0.05$); #: significantly varied from PL ($p < 0.05$); $: significantly varied from *a*-M ($p < 0.05$)
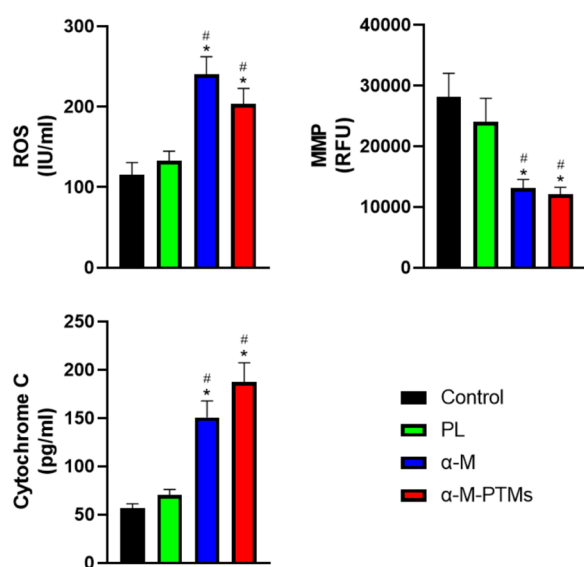
Discussion

α-Mangostin, a primary xanthone found in the pericarps of *Garcinia mangostana,* shows significant anti-proliferative effects on various cancer cells but suffers from low oral bioavailability. Hence, the use of phytosomes as a new nano-based drug delivery system was explored in this study.

Statistical analysis of model fit demonstrated that the selected models exhibit close alignment between adjusted and predicted $R2$ values of less than 0.2 and higher adequate precision values than the desired value of 4, indicating a robust signal-to-noise ratio. The lack-of-fit *P*-values confirm the model's adequacy. As a result, the selected models might be a good fit for exploring the experimental design space. Diagnostic plots further validate the models' fit, showing well-distributed residuals that suggests the absence of constant error and strong correlation between actual and predicted values of the three responses that indicates the appropriateness of the models and their suitability for exploring the experimental design space [16, 22, 23].

The prepared *α*-M-PTMs ranged in size from 103.2 to 327.3 nm. The vesicle size of the suggested *α*-M-PTMs was modified to the lowest value since augmenting the surface area accessible for penetration through particle size reduction could improve tumor penetration. It is reported that lipidic systems with a size less than 400 can be preferentially accumulated within solid malignant tissues [24–27].

The *α*-M:PL molar ratio and process temperature significantly influence vesicle size. The direct relationship between *α*-M: PL molar ratio may be related to the increase in the relative PL amount in the formulation, which is considered the building unit of the proposed PTMs. Thus, increasing the PL amount could promote the formation of large-sized vesicles [28]. A similar direct relationship between PL amount and PTMs vesicular size has been previously reported [29]. Further, the direct relationship observed in our study was congruent with the results of previously reported vesicular systems in general [30]. For instance, PL amount was directly related to the vesicle size of ethosomes loaded with antipsoriatic drugs [31]. For instance, the amount of PL was directly correlated with lipid-based vesicular size [31]. In a different study, it was discovered that increasing the concentration of PL increased the size of the vesicle that contained avanafil invasomes [23]. Smaller particles were seen at higher temperatures when considering the impact of temperature. This finding was consistent with earlier investigations that prepared PTMs [32]. The *α*-M-PTMs demonstrated reasonable PDI values, ranging from 0.209 to 0.417. PDI is a numerical parameter ranging from zero to one that indicates particle size distribution homogeneity. Values approaching zero indicate extremely monodispersed particles, whereas those approaching one indicate highly polydispersed and heterogenous systems [33]. PDI of less than 0.5 is generally acceptable in pharmaceutical formulations [33, 34].

Both *α*-M: PL molar ratio and process temperature positively affect encapsulation, supported by the positive

signs of their linear terms in the developed equation. The increased encapsulation at higher α-M: PL molar ratios could be related to the increased size of the vesicles leading to entrapping more activity within the lipid bilayers. In addition, the lipophilicity of α-M could contribute to this observation. Owing to its highly lipophilic nature, α-M is anticipated to become enmeshed in the lipid phase. Accordingly, increasing the PL amount increases the number of lipid particles forming each vesicle, increasing the chances of active integration within the vesicular lipid content [31, 35]. Concerning the process temperature effect, it is worth noting that the integration of α-M within the prepared PTMs with increasing temperature coincides with previous studies [30].

The observed responses of the optimized formulation agreed with the anticipated ones, with relative percentage errors of 2.72, 1.37, and 1.46% for size, PDI, and EE%, respectively. The low relative-percentage error for all responses demonstrates the optimization procedure's reliability. Additionally, the optimized formulation's mean zeta potential was -44.5 ± 1.5 mV and exhibited almost spherical entities. The negative zeta potential could be attributed to the negatively charged phospholipid involved in the complex formation. In addition, the measured absolute value was greater than 30 indicating the stability of the formed dispersion against aggregation [36].

In the cytotoxic assay against SKOV 3 human ovary tumor cells, α-M-PTMs significantly enhanced cytotoxicity with an IC50 of 2.14 μg/ml, compared to α-M's IC50 of 5.90 μg/ml, reducing α-M's IC50 by about 64% when incorporated into PTMs. This is consistent with several reports describing the positive impact of PTMs on the cytotoxic activities of natural molecules [37, 38]. In general, the anti-proliferative activities of xanthones including α-M have been linked to its hydroxyl groups [39]. In particular, their pro-apoptotic activity has been shown to involve modulation of MAPK pathways leading to apoptosis and inhibition of cellular proliferation [40].

The results also showed a significant increase in the sub-G1 cell population for cells treated with α-M-PTMs compared to the control, with lesser increases for PL and α-M treatments. Additionally, α-M notably caused S phase cell cycle arrest. The S phase is a stage in the cell cycle where DNA replication occurs. This finding is consistent with previous studies [41] and suggests that α-M has the potential to interfere with DNA replication in SKOV-3 cells. On the other hand, it was observed that α-M-PTMs cause decrease in cell fraction in the S phase. This can be explained in light of the ability of low concentrations of α-M to enhance cell accumulation in the S phase while higher concentrations resulted in reduction of cellular population the S phase [42]. This primarily

indicates the ability of α-M-PTMs to deliver higher concentration of α-M into SKOV-3 cells. Overall, these findings indicate that treatment with α-M-PTMs impacts the cell-cycle distribution of SKOV 3 cells, mainly in the sub-G1 stage. Consistently, the delivery of cytotoxic drugs through nanoparticles has been previously associated with cell cycle arrest at the sub-G1 phase [43]. The intracellular bioavailability of cytotoxic compounds influences their effects on the cell cycle phases [44]. The increased cytotoxic activity of α-M-PTMs appears to have promoted cell cycle arrest at the sub-G1 phase in comparison to S phase arrest observed with the raw α-M. It appears that as the intracellular concentration of α-M increases, SKOV-3 cells are more prone to encounter cell cycle arrest at the sub-G1 phase, which is an early stage of the cell cycle [45–47].

Studies have revealed that certain compounds that cause cell cycle arrest during the sub-G1 phase can subsequently promote cancer cells` apoptosis [48]. Using annexin V and PI labeling, the study found that α-M-PTMs significantly increased late apoptosis in SKOV-3 cells. This is supported by several studies highlighting the ability of α-M to provoke apoptosis in SKOV-3 and other ovarian cancer cells [49–51]. Our data is also consistent with previous studies that showed the ability of α-M to particularly enhance late apoptosis in oral squamous cell carcinoma cells [52]. Evading apoptosis is a hallmark of cancer; hence the pro-apoptotic potential of cytotoxic drugs is a critical parameter for assessing their anticancer activities [53]. In this regard, the apoptotic activity of α-M was significantly enhanced when incorporated into the PTMs formulation, suggesting improved cellular bioavailability and potentially therapeutic effects [54].

Apoptosis is controlled by crucial proteolytic enzymes and regulatory proteins [55]. The levels of these apoptotic regulators are often altered in cancer cells to enable tumor growth and evade apoptosis [55]. Therefore, any compound that has the potential to reverse these antiapoptotic changes is a promising drug candidate. In the present study, α-M has induced pro-apoptotic alterations in the levels of TP53, CASP3, BAX, and BCL2, in SKOV 3 cells, and its activity was significantly enhanced by the PTMs formulation. These findings are also consistent with the reported apoptotic activities of α-M as it was shown to induce pro-apoptotic expression levels of CASP3, BAX, and BCL2 in several studies [41, 56]. It is noteworthy to report that phytosomal uptake was previously shown to upregulate caspase 3 and BAX encoding pro-apoptotic genes [57]. The enhanced pro-apoptotic activity of α-M-PTMs observed in the current study can be explained based on increased cellular uptake pf phytosomes via internalization that is proposed to partly

implicate phagocytosis and caveolae-mediated endocytosis pathways [58].

Finally, α-M-PTMs significantly increased ROS, disrupted mitochondrial function, and enhanced cytochrome c release in SKOV-3 cells. Increased ROS generation with mitochondrial damage is a critical driver of the intrinsic apoptosis pathway [59, 60]. MMP loss leads to alterations in BAX and BCL2 expression, which induces the cytochrome c cytoplasmic release from the mitochondria [61]. Releasing cytochrome c results in caspase activation and eventually cell death [62, 63]. Overall, the results of this study showed that α-M-PTMs displayed a notable induction of oxidative damage, apoptosis, and mitochondrial dysfunction which is in line with the reported activities of α-M in cancer cells [64–66].

Conclusion

The present study highlighted the significant potential of the phytosome formulation to improve the cytotoxic activity of α-M against SKOV-3 cells. The results of cell cycle analysis and annexin V staining indicated that apoptosis was enhanced. The formula improved the physiochemical and biological characteristics of α-M-PTMs in inducing oxidative damage and the intrinsic mitochondria-dependent apoptosis pathway. It induced pro-apoptotic alterations in the TP53, CASP3, BCL2, and BAX expression levels in SKOV 3 cells. In general, these results indicate that integrating α-M into the formulated phytosome presents a promising therapeutic approach in addressing breast cancer, but verification of these findings is required through in vivo animal studies. Furthermore, exploring the efficacy of the α-M-PTMs formula on different cancer cell lines will be a key objective for future research endeavors.

Abbreviations

ANOVA	Analysis of variance
BAX	BCL2 associated X, apoptosis regulator
BCL2	B-cell leukemia/lymphoma 2
CASP3	Caspase-3
DLS	Dynamic light scattering
DMEM	Dulbecco's modified-eagle's medium
EA.hy926	Human umbilical vein cell line
EE	Entrapment efficiency
FACS	Fluorescence-activated cell sorting
FBS	Fetal bovine serum
FTIR	Fourier-transform infrared
α-M	α-Mangostin
α-M-PTMs	α-Mangostin-phytosomes formula
MMP	Mitochondrial membrane potential
mRNA	Messenger ribonucleic acid
PBS	Phosphate-buffered saline
PCR	Polymerase chain reaction
PDI	Polydispersity index
PI	Propidium iodide
PL	Phospholipid
PRESS	Predicted-residual sum of squares
PTMs	Phytosomes
ROS	Reactive oxygen species
SKOV 3	Ovarian cancer cell line
SRB	Sulforhodamine B
TP53	Tumor protein p53

Supplementary Information

The online version contains supplementary material available at https://doi.org/10.1186/s43094-024-00718-x.

Additional file1 (DOCX 321 KB)

Author contributions
Conceptualization, H.M.A., H.Z.A., and M.Y.A.; methodology, A.J.A., S.M.B., S.E.E., S.R.M.I. and G.A.M.; software, S.M.B., and O.A.A; validation, O.A.A, S.M.B. and A.J.A.; formal analysis, A.J.A. and S.E.E.; writing—original draft preparation, H.M.A., S.M.B., A.B.A. and A.J.A.; writing—review and editing, H.M.A., S.M.B., A.B.A. and A.J.A.; supervision, H.M.A.; project administration, H.M.A.; funding acquisition, H.M.A., All authors have read and agreed to the published version of the manuscript.

Availability of data and material
The data supporting this work are accessible upon reasonable request from the corresponding author.

Declarations

Ethics approval and consent to participate
Not applicable.

Consent for publication
Not applicable.

Competing interests
The authors state that there are no known competing financial interests or personal relationships that could have appeared to affect the work presented in this paper.

Author details
[1]Department of Pharmacology and Toxicology, Faculty of Pharmacy, King Abdulaziz University, 21589 Jeddah, Saudi Arabia. [2]Department of Pharmaceutics, Faculty of Pharmacy, King Abdulaziz University, 21589 Jeddah, Saudi Arabia. [3]Biology Department, Faculty of Science, King Khalid University, Abha, Saudi Arabia. [4]Cell Culture Lab, Egyptian Organization for Biological Products and Vaccines (VACSERA Holding Company), 51 Wezaret El-Zeraa St., Agouza, Giza, Egypt. [5]Department of Clinical Microbiology and Immunology, Faculty of Medicine, King Abdulaziz University, 21589 Jeddah, Saudi Arabia. [6]Department of Natural Products and Alternative Medicine, Faculty of Pharmacy, King Abdulaziz University, 21589 Jeddah, Saudi Arabia. [7]Preparatory Year Program, Department of Chemistry, Batterjee Medical College, 21442 Jeddah, Saudi Arabia.

References

1. Chen J, Karmakar B, Salem MA, Alzahrani AY, Bani-Fwaz MZ, Abdel-Daim MM, El-kott AF (2022) CuO NPs@Starch as a novel chemotherapeutic drug for the treatment of several types of gastrointestinal system cancers including gastric, pancreatic, and colon cancers. Arab J Chem 15:103681
2. Carioli G, Malvezzi M, Bertuccio P, Hashim D, Waxman S, Negri E, Boffetta P, La Vecchia C (2019) Cancer mortality in the elderly in 11 countries worldwide, 1970–2015. Ann Oncol 30(8):1344–1355
3. Morikawa A, Kawabata A, Shirahige K, Akiyama T, Okamoto A, Sutani T (2022) Altered cervicovaginal microbiota in premenopausal ovarian cancer patients. Gene 811:146083
4. Pan R, Chen Y, Nandakumar KS, Chen Y (2022) Gancao Nurish-Yin Decoction medicated serum inhibits growth and migration of ovarian cancer cells: network pharmacology-based analysis and biological validation. Pharmacol Res - Mod Chin Med 2:100062
5. Zhang M, Xia B, Xu Y, Zhang Y, Xu J, Lou G (2019) Circular RNA (hsa_circ_0051240) promotes cell proliferation, migration and invasion in ovarian cancer through miR-637/KLK4 axis. Artif Cells Nanomed Biotechnol 47(1):1224–1233
6. Li C, Yang Y, Wang H, Song Y, Huang H (2022) miR-362-3p suppresses ovarian cancer by inhibiting LRP8. Transl Oncol 15(1):101284
7. Abdallah HM, El-Bassossy HM, Mohamed GA, El-Halawany AM, Alshali KZ, Banjar ZM (2016) Phenolics from *Garcinia mangostana* alleviate exaggerated vasoconstriction in metabolic syndrome through direct vasodilatation and nitric oxide generation. BMC Complement Altern Med 16(1):1–10
8. Mohamed GA, Al-Abd AM, El-Halawany AM, Abdallah HM, Ibrahim SR (2017) New xanthones and cytotoxic constituents from *Garcinia mangostana* fruit hulls against human hepatocellular, breast, and colorectal cancer cell lines. J Ethnopharmacol 198:302–312
9. Ibrahim SR, Abdallah HM, El-Halawany AM, Radwan MF, Shehata IA, Al-Harshany EM, Zayed MF, Mohamed GA (2018) Garcixanthones B and C, new xanthones from the pericarps of *Garcinia mangostana* and their cytotoxic activity. Phytochem Lett 25:12–16
10. Ibrahim MY, Hashim NM, Mariod AA, Mohan S, Abdulla MA, Abdelwahab SI, Arbab IA (2016) *α*-Mangostin from *Garcinia mangostana* Linn: an updated review of its pharmacological properties. Arab J Chem 9(3):317–329
11. Meylina L, Muchtaridi M, Joni IM, Mohammed AFA, Wathoni N (2021) Nanoformulations of *α*-mangostin for cancer drug delivery system. Pharmaceutics 13(12):1993
12. Zhang K-j, Gu Q-l, Yang K, Ming X-j, Wang J-x (2017) Anticarcinogenic effects of *α*-mangostin: a review. Planta Med 83(03/04):188–202
13. Li J, Wang X, Zhang T, Wang C, Huang Z, Luo X, Deng Y (2015) A review on phospholipids and their main applications in drug delivery systems. Asian J Pharm Sci 10(2):81–98
14. Ghanbarzadeh B, Babazadeh A, Hamishehkar H (2016) Nano-phytosome as a potential food-grade delivery system. Food Biosci 15:126–135
15. Azeez NA, Deepa VS, Sivapriya V (2018) Phytosomes: emergent promising nano vesicular drug delivery system for targeted tumor therapy. Adv Nat Sci: Nanosci Nanotechnol 9(3):033001
16. Pan-In P, Wongsomboon A, Kokpol C, Chaichanawongsaroj N, Wanichwecharungruang S (2015) Depositing *α*-mangostin nanoparticles to sebaceous gland area for acne treatment. J Pharmacol Sci 129(4):226–232
17. Alamoudi AJ, Badr-Eldin SM, Ahmed OA, Fahmy UA, Elbehairi SEI, Alfaifi MY, Asfour HZ, Mohamed GA, Ibrahim SR, Abdel-Naim AB (2023) Optimized bilosome-based nanoparticles enhance cytotoxic and pro-apoptotic activity of costunolide in LS174T colon cancer cells. Biomed pharmacother 168:115757
18. Nunez R (2001) DNA measurement and cell cycle analysis by flow cytometry. Curr Issues Mol Biol 3(3):67–70
19. Bashmail HA, Alamoudi AA, Noorwali A, Hegazy GA, AJabnoor G, Choudhry H, Al-Abd AM (2018) Thymoquinone synergizes gemcitabine anti-breast cancer activity via modulating its apoptotic and autophagic activities. Sci Rep 8(1):1–11
20. Wlodkowic D, Skommer J, Darzynkiewicz Z (2009) Flow cytometry-based apoptosis detection. In: Apoptosis: methods and protocols, Second Edition, pp.19–32.
21. Livak KJ, Schmittgen TD (2001) Analysis of relative gene expression data using real-time quantitative PCR and the 2−∆∆CT method. Methods 25(4):402–408
22. Alhakamy NA, Fahmy UA, Badr-Eldin SM, Ahmed OA, Asfour HZ, Aldawsari HM, Algandaby MM, Eid BG, Abdel-Naim AB, Awan ZA (2020) Optimized icariin phytosomes exhibit enhanced cytotoxicity and apoptosis-inducing activities in ovarian cancer cells. Pharmaceutics 12(4):346
23. Ahmed OA, Badr-Eldin SM (2019) Development of an optimized avanafil-loaded invasomal transdermal film: ex vivo skin permeation and in vivo evaluation. Int J Pharm 570:118657
24. Al-Mahallawi AM, Abdelbary AA, Aburahma MH (2015) Investigating the potential of employing bilosomes as a novel vesicular carrier for transdermal delivery of tenoxicam. Int J Pharm 485(1–2):329–340
25. Pourmahdi N, Sarrafi AH, Larki A (2019) Carbon dots green synthesis for ultra-trace determination of ceftriaxone using response surface methodology. J Fluoresc 29(4):887–897
26. Sharma S, Shukla P, Misra A, Mishra PR (2014) Interfacial and colloidal properties of emulsified systems: pharmaceutical and biological perspective. Colloid and interface science in pharmaceutical research and development. Elsevier, Amsterdam, pp 149–172
27. Yingchoncharoen P, Kalinowski DS, Richardson DR (2016) Lipid-based drug delivery systems in cancer therapy: what is available and what is yet to come. Pharmacol Rev 68(3):701–787
28. Badr-Eldin SM, Aldawsari HM, Ahmed OA, Alhakamy NA, Neamatallah T, Okbazghi SZ, Fahmy UA (2021) Optimized semisolid self-nanoemulsifying system based on glyceryl behenate: a potential nanoplatform for enhancing antitumor activity of raloxifene hydrochloride in MCF-7 human breast cancer cells. Int J Pharm 600:120493
29. Zhang YR, Lin R, Li HJ, He WI DuJZ, Wang J (2019) Strategies to improve tumor penetration of nanomedicines through nanoparticle design. Wiley Interdiscip Rev: Nanomed Nanobiotech 11(1):e1519
30. Thomas L, Viswanad V (2012) Formulation and optimization of clotrimazole-loaded proniosomal gel using 32 factorial design. Sci Pharm 80(3):731–748
31. Dubey V, Mishra D, Dutta T, Nahar M, Saraf D, Jain N (2007) Dermal and transdermal delivery of an anti-psoriatic agent via ethanolic liposomes. J Controlled Release 123(2):148–154
32. Nandhini S, Ilango K (2021) Development and characterization of a nano-drug delivery system containing vasaka phospholipid complex to improve bioavailability using quality by design approach. Res Pharma Sci 16(1):103
33. El Taweel MM, Aboul-Einien MH, Kassem MA, Elkasabgy NA (2021) Intranasal zolmitriptan loaded-bilosomes with extended nasal mucociliary transit time for direct nose to brain delivery. Pharmaceutics 13(11):1828
34. Haghighi P, Ghaffari S, Arbabi Bidgoli S, Qomi M, Haghighat S (2018) Preparation, characterization and evaluation of Ginkgo biloba solid lipid nanoparticles. Nanomed Res J 3(2):71–78
35. Chin GS, Todo H, Kadhum WR, Hamid MA, Sugibayashi K (2016) In vitro permeation and skin retention of *α*-mangostin proniosome. Chem Pharm Bull 64(12):1666–1673
36. Shriram RG, Moin A, Alotaibi HF, Khafagy E-S, Al Saqr A, Abu Lila AS, Charyulu RN (2022) Phytosomes as a plausible nano-delivery system for enhanced oral bioavailability and improved hepatoprotective activity of silymarin. Pharmaceuticals 15(7):790
37. Govindaram LK, Bratty MA, Alhazmi HA, Kandasamy R, Thangavel N, Ibrahim AM, Mariya GA, Kumar P (2022) Formulation, biopharmaceutical evaluation and in-vitro screening of polyherbal phytosomes for breast cancer therapy. Drug Dev Ind Pharm 48(10):552–565
38. Al-Samydai A, Qaraleh MA, Alshaer W, Al-Halaseh LK, Issa R, Alshaikh F, Abu-Rumman A, Al-Ali H, Al-Dujaili EA (2022) Preparation, characterization, wound healing, and cytotoxicity assay of PEGylated nanophytosomes loaded with 6-gingerol. Nutrients 14(23):5170
39. Matsumoto K, Akao Y, Ohguchi K, Ito T, Tanaka T, Iinuma M, Nozawa Y (2005) Xanthones induce cell-cycle arrest and apoptosis in human colon cancer DLD-1 cells. Biorg Med Chem 13(21):6064–6069
40. Itoh T, Ohguchi K, Iinuma M, Nozawa Y, Akao Y (2008) Inhibitory effect of xanthones isolated from the pericarp of *Garcinia mangostana* L. on rat basophilic leukemia RBL-2H3 cell degranulation. Biorg Med Chem 16(8):4500–4508
41. Zhu X, Li J, Ning H, Yuan Z, Zhong Y, Wu S, Zeng J-Z (2021) *α*-Mangostin induces apoptosis and inhibits metastasis of breast cancer cells via regulating RXR*α*-AKT signaling pathway. Front Pharmacol 12:739658

42. Rojas-Ochoa A, Córdova EJ, Carrillo-García A, Lizano M, Pedraza-Chaverri J, Patiño N, Cruz-Gregorio A, Osnaya N (2021) The polyphenols *α*-mangostin and nordihydroguaiaretic acid induce oxidative stress, cell cycle arrest, and apoptosis in a cellular model of medulloblastoma. Molecules 26(23):7230

43. Maroufi NF, Vahedian V, Mazrakhondi SAM, Kooti W, Khiavy HA, Bazzaz R, Ramezani F, Pirouzpanah SM, Ghorbani M, Akbarzadeh M (2020) Sensitization of MDA-MBA231 breast cancer cell to docetaxel by myricetin loaded into biocompatible lipid nanoparticles via sub-G1 cell cycle arrest mechanism. Naunyn-Schmiedeberg's Arch Pharmacol 393:1–11

44. Sakaue-Sawano A, Kobayashi T, Ohtawa K, Miyawaki A (2011) Drug-induced cell cycle modulation leading to cell-cycle arrest, nuclear mis-segregation, or endoreplication. BMC Cell Biol 12(1):1–12

45. Richon VM, Sandhoff TW, Rifkind RA, Marks PA (2000) Histone deacetylase inhibitor selectively induces p21WAF1 expression and gene-associated histone acetylation. Proc Natl Acad Sci 97(18):10014–10019

46. Itharat A, Rattarom R, Hansakul P, Sakpakdeejaroen I, Ooraikul B, Davies NM (2021) The effects of Benjakul extract and its isolated compounds on cell cycle arrest and apoptosis in human non-small cell lung cancer cell line NCI-H226. Res Pharma Sci 16(2):129

47. Peng B-Y, Singh AK, Chan C-H, Deng Y-H, Li P-Y, Su C-W, Wu C-Y, Deng W-P (2023) AGA induces sub-G1 cell cycle arrest and apoptosis in human colon cancer cells through p53-independent/p53-dependent pathway. BMC Cancer 23(1):1–13

48. Kazemi M, Kouhpeikar H, Delbari Z, Khodadadi F, Gerayli S, Iranshahi M, Mosavat A, Rassouli FB, Rafatpanah H (2021) Combination of auraptene and arsenic trioxide induces apoptosis and cellular accumulation in the subG1 phase in adult T-cell leukemia cells. Iran J Basic Med Sci 24(12):1643

49. Ittiudomrak T, Puthong S, Roytrakul S, Chanchao C (2019) *α*-Mangostin and apigenin induced cell cycle arrest and programmed cell death in SKOV-3 ovarian cancer cells. Toxicol Res 35:167–179

50. Borzdziłowska P, Bednarek I (2022) Alpha mangostin and cisplatin as modulators of exosomal interaction of ovarian cancer cell with fibroblasts. Int J Mol Sci 23(16):8913

51. Borzdziłowska P, Bednarek I (2022) The effect of *α*-mangostin and cisplatin on ovarian cancer cells and the microenvironment. Biomedicines 10(5):1116

52. Kwak H-H, Kim I-R, Kim H-J, Park B-S, Yu S-B (2016) *α*-Mangostin induces apoptosis and cell cycle arrest in oral squamous cell carcinoma cell. Evid-based Complement Altern Med 2016:5352412

53. Ali A, Kulik G (2021) Signaling pathways that control apoptosis in prostate cancer. Cancers 13(5):937

54. Kidd PM (2009) Bioavailability and activity of phytosome complexes from botanical polyphenols: the silymarin, curcumin, green tea, and grape seed extracts. Altern Med Rev 14(3):226–246

55. Lu X, Chen D, Yang F, Xing N (2020) Quercetin inhibits epithelial-to-mesenchymal transition (EMT) process and promotes apoptosis in prostate cancer via downregulating lncRNA MALAT1. Cancer Manag Res 12:1741

56. Kaomongkolgit R, Chaisomboon N, Pavasant P (2011) Apoptotic effect of alpha-mangostin on head and neck squamous carcinoma cells. Arch Oral Biol 56(5):483–490

57. Wongkaewkhiaw S, Wongrakpanich A, Krobthong S, Saengsawang W, Chairoungdua A, Boonmuen N (2022) Induction of apoptosis in human colorectal cancer cells by nanovesicles from fingerroot (*Boesenbergia rotunda* (L.) Mansf.). PLoS ONE 17(4):e0266044

58. Kadriya A, Falah M (2023) Nanoscale phytosomes as an emerging modality for cancer therapy. Cells 12(15):1999

59. Lemasters JJ (1999) V. Necrapoptosis and the mitochondrial permeability transition: shared pathways to necrosis and apoptosis. Am J Physiol, Gastrointest Liver Physiol 276(1):1–6

60. Crompton M (1999) The mitochondrial permeability transition pore and its role in cell death. Biochem J 341(2):233–249

61. Kim J-Y, Park J-H (2003) ROS-dependent caspase-9 activation in hypoxic cell death. FEBS Lett 549(1–3):94–98

62. Ly J, Grubb D, Lawen A (2003) The mitochondrial membrane potential (deltapsi (m)) in apoptosis; an update. Apoptosis 8(2):115–128

63. Yang J, Liu X, Bhalla K, Kim CN, Ibrado AM, Cai J, Peng T-I, Jones DP, Wang X (1997) Prevention of apoptosis by Bcl-2: release of cytochrome c from mitochondria blocked. Science 275(5303):1129–1132

64. Lee C-H, Ying T-H, Chiou H-L, Hsieh S-C, Wen S-H, Chou R-H, Hsieh Y-H (2017) Alpha-mangostin induces apoptosis through activation of reactive oxygen species and ASK1/p38 signaling pathway in cervical cancer cells. Oncotarget 8(29):47425

65. Cruz-Gregorio A, Aranda-Rivera AK, Aparicio-Trejo OE, Medina-Campos ON, Sciutto E, Fragoso G, Pedraza-Chaverri J (2023) α-Mangostin induces oxidative damage, mitochondrial dysfunction, and apoptosis in a triple-negative breast cancer model. Phytother Res 37:3394–3407

66. Alam M, Rashid S, Fatima K, Adnan M, Shafie A, Akhtar MS, Ganie A, Eldin SM, Islam A, Khan I (2023) Biochemical features and therapeutic potential of *α*-mangostin: mechanism of action, medicinal values, and health benefits. Biomed pharmacother 163:114710

Publisher's Note